Journal Name

ARTICLE

$FeOx/Al_2O_3$ catalysts for high-temperature decomposition of N_2O under conditions of NH_3 oxidation in nitric acid production

Received 00th January 20xx,
Accepted 00th January 20xx

DOI: 10.1039/x0xx00000x

www.rsc.org/

Galina Sádovská[a,b], Edyta Tabor[a,*], Milan Bernauer[a], Petr Sazama[a], Vlastimil Fíla[c], Tomáš Kmječ[d], Jaroslav Kohout[d], Karel Závěta[d], Věnceslava Tokarová[e], Zdeněk Sobalík[a]

The catalytic activity of a series of $FeOx/Al_2O_3$ prepared under various conditions was evaluated for high temperature decomposition of N_2O (HT-deN_2O) in the complex gas mixture produced by oxidation of ammonia. Thus the relevant step in the industrial nitric acid production process was simulated. The catalyst stability during a long exposure (12 days) to reaction conditions relevant to HT-deN_2O was studied. Both fresh and aged FeO_x/Al_2O_3 exhibited more than 90 % conversion of N_2O in the 750-900 °C temperature range. Structural analysis showed that prepared FeO_x/Al_2O_3 catalysts contained various proportions of δ, θ and α alumina phases and up to four individual iron speciations. In the δ and θ Al_2O_3 phases well stabilized Fe(III) in T_d or O_h coordination were identified as the active species in HT-deN_2O.

1. Introduction

The efficient elimination of N_2O from the exhaust of the nitric acid production, based on ammonia oxidation, represents one of the essential challenges for environmentally friendly large-scale production of the acid. A capable and efficient process of N_2O elimination is indispensable for the industry because of the potential contribution of the N_2O to global warming.[1, 2] The newly proposed alternative technique of direct N_2O catalytic decomposition immediately after the ammonia burners has shown great promise.[3, 4] Such an approach minimizes the economic demands for the process and at the same time allows relatively convenient approach for retrofitting the existing technology. Nevertheless, this approach exposes any potential catalysts to very harsh conditions such as the high temperatures of approximately 750–930 °C and to a gas mixture containing not only 700−2000 ppm of N_2O but also 10 vol.% of NO, 15 vol.% of H_2O and approximately 2 vol.% of O_2.[1, 2, 5, 6] These conditions require the use of efficient and highly stable catalysts to fulfil the requirements for long-term stability for the typical space velocity of approximately 100 000 h^{-1}. At the same time, the expense of the preparation of such new catalysts should be sufficiently low to be economically viable for the industry, excluding any use of noble-metal-containing catalysts.

Iron-containing catalysts, particularly iron zeolites have been highly efficient for N_2O decomposition.[7] However, their long-term stability, under the specific conditions of the high-temperature N_2O decomposition (HT-deN_2O) process, is still questionable. On the other hand, adequate long-term stability has been demonstrated for the alumina-supported iron catalysts which provide a relatively inexpensive alternative, albeit one with a lower activity than the zeolites. FeO_x/Al_2O_3 catalysts have also been considered for the N_2O decomposition over the noble-metal-free catalysts by Konsolakis *et al.*[8] The potential of using iron-based catalysts for N_2O decomposition was recently demonstrated by Pinaeva *et al.*[9] The real potential of FeO_x/Al_2O_3 catalysts for the HT-deN_2O process was clearly demonstrated by the work of Giecko *et al.*[6]

A literature overview of the applications of the FeO_x/Al_2O_3 catalysts and their relevance for the HT-deN_2O process is presented in Table 1, showing the typical compositions of the studied catalysts and the experimental conditions of the performed tests.

With only two exceptions, the experiments described in Table 1 were performed using a simplified mixture of N_2O with an inert gas and did not measure the long-term efficiency of the catalysts; however, some experiments have been performed in the temperature region of 700−900 °C. Moreover, the iron content, used in the N_2O decomposition experiments summarized in Table 1 varied substantially from 1 to 100 wt. %.

[a] *J. Heyrovský Institute of Physical Chemistry of the Czech Academy of Sciences, Dolejškova 2155/3, CZ-182 23 Prague 8, Czech Republic*
**Email:edyta.tabor@jh-inst.cas.cz*
[b] *University of Pardubice, Faculty of Chemical Technology, Doubravice 41, CZ-53210 Pardubice, Czech Republic*
[c] *University of Chemistry and Technology, Faculty of Chemical Technology, Technická 5, CZ-166 28 Prague 6, Czech Republic*
[d] *Joint Laboratory for Mössbauer Spectroscopy, Faculty of Mathematics and Physics, Charles University in Prague, V Holešovičkách 2, CZ -180 00 Prague 8, Czech Republic*
[e] *Unipetrol Centre for Research and Education, a.s., Revoluční 84, CZ- 400 01 Ústí nad Labem, Czech Republic*

Electronic Supplementary Information (ESI) available: [details of any supplementary information available should be included here]. See DOI: 10.1039/x0xx00000x

Journal Name

ARTICLE

Table 1 Literature overview of FeO_x/Al_2O_3 catalysts tested for N2O decomposition and comparison to the results of the present work.

Iron content	Preparation	Reaction mixture	React. Temp.	Aging	Ref.
0-5 % Fe	impregnation	N_2O/inert	<600–650 °C	-	10
0-100 % Fe	solid state	N_2O/inert	<600–650 °C	-	11, 12
1–10% Fe	impregnation	N_2O/inert	700–900 °C	-	13
42–72 wt% Fe_2O_3	co-precipitation	$N_2O/O_2/NO/H_2O$ in He	700-900 °C	yes	6
2.0 wt% Fe	co-precipitation	N_2O/O_2/inert	Up to 600 °C	-	14
6.0 wt% Fe	ion exchange	N_2O/O_2/inert	700–900 °C	-	15
78.9% Fe_2O_3	co-precipitation	N_2O/NO/inert	700–900 °C	yes	16
0.86–19.8 wt% Fe	impregnation	$N_2O/O_2/H_2O$ in He	700–900 °C	-	9
1 – 10 wt% Fe	impregnation	$N_2O/O_2/NO/H_2O$ in He	400–900 °C	yes	present work

Boubnov *et al.*[17] mainly focused on the identification of the iron species and their relationship to the various alumina forms. Their analysis was mostly related to the δ-alumina, which is actually not realistic because the working temperature of the HT-deN_2O process is mainly above the temperature region of the existence of the δ polymorph. There is much evidence that the alumina modifications influenced the speciation of active species and therefore the catalytic properties of the resulting alumina-supported catalyst. [17, 18] Therefore, the identity of the alumina support phase is highly relevant. Actually, Al_2O_3 forms various metastable polymorphs over a wide range of temperatures: face-centred-cubic structures of the γ-, δ-, σ- and η-Al_2O_3; monoclinic and orthorhombic structures of ϑ- and ι-Al_2O_3, respectively; the hexagonal close-packed structure of κ-, χ-Al_2O_3, and finally the thermodynamically stable phase α-Al_2O_3 (corundum) forms at high temperatures.[19] Due to the complexity of the alumina structures, their transformations, and the role of several crucial parameters (temperature history, humidity and the effect of transition metal cations (including iron)), the state of the alumina as a support and its further development during the long-term exposure to high-temperature conditions cannot be easily predicted. [8, 9, 17-19]

The prevailing evidence suggests that in the temperature region of 800–950 °C used for HT-N_2O decomposition, alumina support coexists in several polymorphs, namely δ, ϑ and α forms.[19, 20] A prominent role of the most stable transitional ϑ-Al_2O_3 form and the structure with the equal occurrence of octahedral (O_h) and tetrahedral (T_d) Al^{3+} sites have been anticipated in the HT-deN_2O process.[21] To make the problem even more complex, the presence of an amorphous phase or low-crystallinity component(s) after the böhmite calcination cannot be excluded. A summary of the types of iron

species formed on alumina support can be presented as follows: isolated Fe(III) species, less specifically defined as 'strongly associated iron (III)' species, highly dispersed Fe(III) incorporated into the alumina structure by occupying Al sites, ferric oxide species with different nuclearity, including FeO_x dimer/oligomer aggregates and FeO_x nanoparticles.[6, 9, 16, 19, 21] [10] In the case of the samples with higher iron content, the identified structures also contain Fe_2O_3 particles. In some cases, the formation of mixed oxides in the form of $Al_{2-x}Fe_xO_3$ phase is also proposed. The possible formation of a monolayer of FeO_x over the γ-Al_2O_3 was suggested by Xie *et al.*[22] without a detailed structural analysis of the FeO_x species.

Accordingly, depending on the iron content in the sample, the forms of iron species varied between isolated species, through the 2-D oligomers, 3-D nanoparticles and up to bulk iron oxide particles with the increasing Fe content.[15]

The present study aims at the potential application of FeO_x/Al_2O_3 catalysts for the specific conditions of the HT-deN_2O process along these lines: i) the comparison of three preparation routes using the böhmite-type material or amorphous AlO(OH) suspension as the alumina source ii) the evaluation of the stability of the prepared catalysts during a long exposure to reaction conditions simulating HT-N_2O decomposition; iii) detailed structural analysis of the catalysts in order to characterize the iron active structures and conditions for their optimal formation.

2. Catalysts preparation and characterization

2.1 Catalysts preparation

Three series of FeO_x catalysts supported on alumina treated at various temperatures or on hydrated amorphous aluminium oxide AlO(OH) are studied. Fe/Al_2O_3-A and Fe/Al_2O_3-B catalysts were prepared by impregnation of böhmite (Fe/Al_2O_3-A) and alumina (Fe/Al_2O_3-B) with aqueous solution of ammonium iron(III) citrate. The Fe/Al_2O_3-C catalyst was prepared by the impregnation of amorphous aluminium oxide AlO(OH) using an acidic $FeCl_2$ solution as source of iron. The amorphous aluminium oxide AlO(OH) was prepared by precipitation of

ammonium aluminium sulphate by ammonia. Details of the preparation procedures are described in the Supplementary Information. Selected catalysts were hydrothermally aged for 12 days at 800 °C in the stream of gas mixture of 700–2000 ppm of N_2O, 10 vol.% of NO, 15 vol.% of H_2O and 2 vol.% of O_2 formed after the oxidation of NH_3 on Pt grid for laboratory simulated HNO_3 production. Aged samples were denoted by "/12".

2.2 Structural analysis

The composition analysis of the prepared catalysts was performed using an X-ray fluorescence spectrometer ARL 9400 XP (Thermo ARL, Switzerland).

The specific surface area was measured by nitrogen adsorption at 77 K using a Micromeritics ASAP 2020 instrument. The samples were evacuated at T = 573 K and at 0.1 mbar for 3 hours prior to the measurements. The specific surface area was calculated using the method of Brunauer, Emmett and Teller (BET) and the micropore volume was evaluated using the t-plot method. The BET value was obtained in the range of the relative N_2 pressure (p/p^0) from 0.02 to 0.30 with at least 12 degrees of freedom for the fitting. The crystallographic structures of the prepared samples were characterized by X-ray analysis using a Rigaku MiniFlex600 instrument, Japan at room temperature. For the identification of the formed phases ICDD (PDF-2) crystallographic database was used. Quantitative analysis was performed using the reference intensity ratio (RIR) method. The crystallite size of the identified phases was determined using the method of Halder-Wagner[23] with the broadening calibrated using a standard reference material (lanthanum boride - LaB_6). The amorphous phase content was estimated from the scattered intensity of the crystalline and amorphous phase mixture.

UV–Vis–NIR reflectance spectra of hydrated iron-catalysts were obtained using a Perkin–Elmer Lambda 950 UV–Vis–NIR spectrometer equipped with an integrating sphere for diffuse-reflectance measurements covered with Spectralon, which was used as a reference. The reflectance was recalculated using the Schuster–Kubelka–Munk function $F(R_\infty) = (1 - R_\infty)^2/2R_\infty$, where R_∞ is the diffuse reflectance from a semi-infinite layer.

^{57}Fe Mössbauer spectra of the samples were collected at room and liquid-helium temperatures. ^{57}Co in Rh matrix was used as the source of the γ-rays. Calibration of the spectrometer was carried out using an α-Fe foil. The mass of the self-supported pellets, pressed from powdered samples, was ~50 mg. All spectra were evaluated using the CONFIT fitting software.

2.3 The catalytic activity tests

The catalytic activity tests were performed in a quartz U-shaped fixed-bed flow-through reactor. The inlet gas, simulating the real reaction mixture for the HT-deN_2O process consisted of 1 000 ppm of N_2O, 0.5 vol.% of NO, 2 vol.% of O_2, 10 vol.% of H_2O, and He as an inert. The gas mixture was passed through the catalyst bed using a top inlet to the reactor with the inner diameter of 7 mm over the samples in the form of grains with the particle size of approximately 0.2–0.4 mm. A decreasing temperature sequence from 900 down to 400 °C was used with a stabilization time of 60 min to obtain the steady-state values. The total catalyst volume was always 0.2 cm^3 and at the overall flow rate of 350 cm^3 min^{-1} provided the gas hour space velocity (GHSV) of approximately 100 000 h^{-1} (typical for industrial N_2O decomposition). The N_2O, N_2, and O_2 contents in the inlet and the outlet mixtures were measured using a Hewlett Packard 6090 gas chromatograph. The analyzed mixture was led through a Hayesep column (packed column) for the retention and removal of the water vapour, then through an HP-Plot Q column (30 m × 0.53 mm × 40 μm film thickness) and through a Molecular sieve 5A (30 m × 0.53 mm × 25 μm film thickness) into a thermal conductivity detector (TCD) monitoring the N_2O, N_2, and O_2 concentrations (for more details see Ref. JPCA). The reproducibility of the resulting N_2O conversions values was ±2%.

The catalytic experiments data at constant GHSV were obtained at identical hydrodynamic conditions for all experiments. These data were reprocessed to constant weight hour space velocity (WHSV) in order to establish the relationship between the structural properties and the catalytic activity.

3. Results and discussion

3.1. Properties of the prepared catalysts

The list of the prepared catalysts as well as their chemical compositions and the textural properties are summarized in Table 2. Fe/Al_2O_3-A materials show the highest surface area (up to approximately 65 m^2 g^{-1}). The surface areas of Fe/Al_2O_3-B and C are approximately 50 and 30% lower than that of Fe/Al_2O_3-A samples, respectively. The t-plot method reveals the predominantly mesoporous character of the supports with the negligible micropore volume. S_{BET} decreases slightly with the increasing content of Fe for all measured samples. The aging process has no significant impact on the textural properties of the studied catalysts the surface area of studied samples was changed about 10 % after the aging (Supplementary Information Table S1).

Table 2 Chemical analysis and surface area of studied iron-alumina catalysts.

Type of catalyst	Fe (%)	S_{BET} (m^2 g^{-1})
5Fe/Al_2O_3-A	5.27	65.3
10Fe/Al_2O_3-A	10.22	62.5
1Fe/Al_2O_3-B	0.85	35.8
4Fe/Al_2O_3-B	4.01	33.7
9Fe/Al_2O_3-B	8.78	32.1
4Fe/Al_2O_3-C	3.69	45.1
Al_2O_3*	0.01	41.7

*Böhmite calcined at 1100 °C for 10 h in air.

3.2 X-ray diffraction

The content of ϑ-Al_2O_3 and δ-Al_2O_3 can be readily estimated from the XRD patterns in the angular (2ϑ) range of 42−50°. The individual phases present in all samples, with their assignement based on RIR method, are listed in Table 3. The crystallite size was determined using the Scherrer's equation in the Halder-Wagner method[23] and the calculated values are also listed in Table 3.

Fig. 1 shows a comparison of the diffractograms of Fe/Al_2O_3 prepared with different sources of alumina (A, B, and C) and similar iron loading (~5 wt. %) (~10 wt. % are discussed in the Supplementary Information, chapter 2, Fig. S1). Both, the various sources of alumina and thermal treatments result in

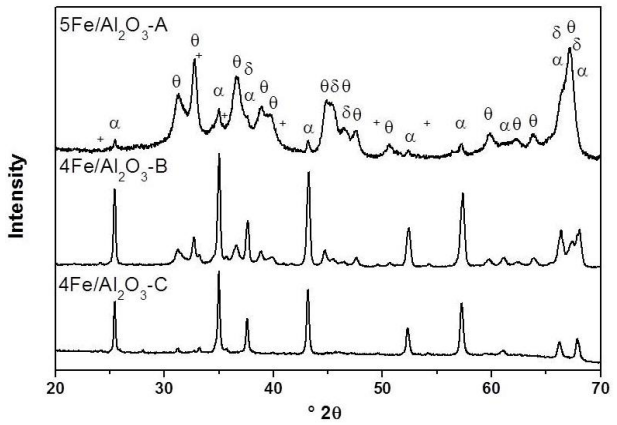

Fig. 1 X-ray diffraction patterns showing the influence of alumina preparation on the content of various alumina polymorphs (the Greek symbols describe alumina polymorphs and crosses Fe_2O_3; Fe content in the catalysts ~ 5 wt.%).

various contents of δ-, ϑ- and α-Al_2O_3 present in the samples, as illustrated in Fig. 1 and Table 3. The calcination of iron-impregnated böhmite at 950 °C (i.e., $5Fe/Al_2O_3$-A), leads to the formation of mostly δ- and ϑ-Al_2O_3, unlike the impregnation of the pre-calcined böhmite at 1100 °C (i.e. $4Fe/Al_2O_3$-B) which contains a high proportion of the α-Al_2O_3 phase. $4Fe/Al_2O_3$-C sample prepared by the impregnation of the amorphous alumina contains mostly α-Al_2O_3 phase, see the result for $4Fe/Al_2O_3$-C.

The diffractograms of Al_2O_3-B with increasing iron loading (0−9 wt. %) are shown in Fig. 2. In the case of the pure böhmite calcined at 1100 °C, a complex mixture of δ, ϑ and α modification is observed with a high proportion of the ϑ phase and only a small amount (< 5%) of the amorphous phase (Table 3). Thermal pretreatment at 1100 °C or calcination of amorphous alumina in the presence of iron leads to the disappearance of the δ modification, preservation of the ϑ-Al_2O_3 modification, and an increasing tendency to the predominant formation of α-Al_2O_3. The higher content of iron on the alumina in the Fe/Al_2O_3-B samples promotes the transformation of alumina to α-Al_2O_3 even above the limit reached by the calcination of the böhmite alone. Böhmite transforms in the sequence of AlO(OH) → δ-Al_2O_3→ ϑ-Al_2O_3 → α-Al_2O_3 when varying the calcination temperatures, and this provides the materials with high-temperature structural stability (resistance to phase transitions), which can be used for supporting the different Fe species (Table 3). The transformation of ϑ- into α-Al_2O_3 in the iron-alumina was accelerated by increasing the iron content (Fig. 2), which is especially pronounced in the detailed comparison of the diffraction lines in the narrow 2ϑ range from 42 to 50° (Fig. 3).[24]

A shift of the α-Al_2O_3 peaks to lower 2 ϑ angles indicates the expansion of the unit cell of the alumina structure (Fig. 3).

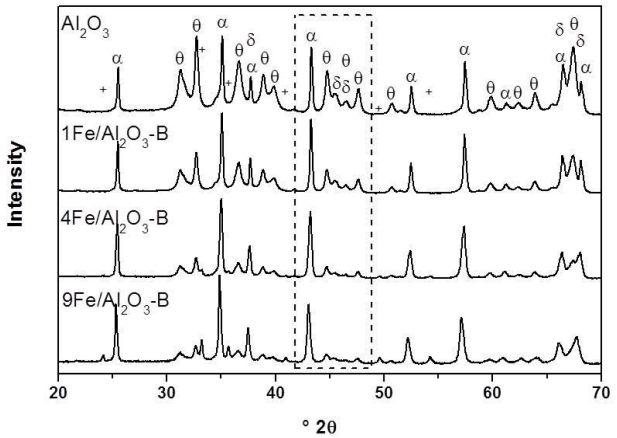

Fig. 2 X-ray diffraction patterns showing the influence of Fe concentration on the content of alumina polymorphs (the Greek symbols correspond to alumina polymorphs and crosses to Fe_2O_3).

Some iron cations can penetrate into the alumina matrix, primarily into α-Al_2O_3, and interchange Al^{3+} ions with the host structure; this effect is observed as the peak shift in the diffractograms. In our case, Fe^{3+} cations with the coordination number of IV and with the ionic radius of 0.49 Å occupied the position of Al^{3+} with the same coordination number but with the lower ionic radius of 0.39 Å. The acceleration of the alumina transformation to the α phase could be assigned to the known ability of iron ions embedded into the alumina structure to decrease the phase-transition temperature. These results confirm that the presence of iron induces the transformation of metastable alumina into the most stable phases or into final α phase.[25-27]

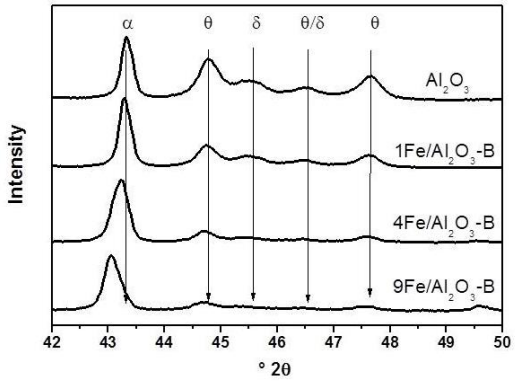

Fig. 3 X-ray diffraction patterns showing the influence of Fe concentration on the final content of the alumina polymorphs present in the alumina precalcined at 1100 °C.

According to the XRD analysis, the preparation route A leads to formation of nano-sized alumina particles with the size of 8-10

nm for δ and ϑ modification in the fresh and 12 days aged samples (Table 3). The sizes of the particles of the α-Al_2O_3 phase increased from 5 to 9 nm after aging. The pure böhmite calcined at 1100 °C transformed into a mixture of δ, ϑ and α-Al_2O_3 particles of ~ 9 nm (Table 3). The similar alumina size parameters can be observed in 1Fe/Al_2O_3-B. The particle sizes were found to be larger than or of the order of 10 nm from XRD data for higher Fe containing samples made by route B. The aging of B-sample led to an increase of α-Al_2O_3 particle size to > 20 nm. No δ-Al_2O_3 phase was detected and the size of ϑ and α-Al_2O_3 particles was 3 and 6 nm, respectively, in the 4Fe/Al_2O_3-C catalyst. Catalysts prepared by the route A showed the Fe_2O_3 particle size of 7 nm for as prepared and 9-17 nm for aged samples. The size of iron oxide particles formed on the alumina matrix obtained by the method B and C is 10-11 nm in all cases. The amount of the amorphous phase of Al_2O_3 was estimated to be less than 10 wt.% for all samples (see Table 3).

Twelve days of aging by exposure to the stream of gas mixture (700–2000 ppm of N_2O, also 10 vol.% of NO, 15 vol.% of H_2O and approximately 2 vol.% of O_2) at 800 °C shows that the transformation of the metastable alumina forms to the α phase is accelerated further, but after the aging the content of the ϑ alumina formed in the Fe/Al_2O_3-A and Fe/Al_2O_3-B catalysts is still high (Supplementary Information, Fig. S2).

3.3 UV-Vis-NIR spectra of Fe/Al_2O_3 catalysts

UV-Vis-NIR spectra are shown in the following figures i) Fig. 4 compares Fe/Al_2O_3-A, -B and -C with a similar Fe content of ~5 wt. %; ii) Fig. 5 shows Fe-Al_2O_3-B with an Fe varying content from 1 to 9 wt.%; iii) Fig. 6 displays the effect of aging on the 10Fe/Al_2O_3-A and 4Fe/Al_2O_3-B samples. The range of NIR spectra comprise the d-d electron transitions of Fe(III) ions [28] in Fe-oxide species typically reflected in a band of low intensity at 11 500 cm^{-1}.[29, 30] In the range of visible light, absorptions due to electron pair transitions (EPT) specific for Fe oxides are characterized by an absorption edge at about 18 000 cm^{-1}. The energy of EPT is higher than that of d-d transition due to the cooperation of two Fe(III) ions mediated by magnetic interaction and is specific for iron oxides. Chernyshova et al.[31] has shown that the energy of the absorption edge gradually increases from ca. 17 800 to 18 500 cm^{-1} with decreasing size of iron oxide from 120 to 7 nm, respectively, like for that of the others oxide clusters. The intense absorption bands in the UV region at 25 000 - 50 000 cm^{-1} generally reflect O→Fe(III) ligand to metal charge-transfer transitions (LMCT) originating from both the ligand oxygens and oxygen atoms in the catalysts support. In contrast to the unambiguous assignment of the absorption edge at about 18 500 cm^{-1}, the assignment of the absorption bands at higher energies to particular Fe species is more complex. The bands at about 28 000 – 31 000 cm^{-1} observed for Fe-zeolites have been ascribed to dinuclear Fe-oxo complexes.[29] However, Pirngruber et al.[32] suggested that it reflects larger Fe-oxo species. Bordiga et al. [33] has assigned the absorptions below 33 000 cm^{-1} to polynuclear Fe-oxo complexes without specified nuclearity. In general an increasing number of Fe-O bonds in the di- and polynuclear Fe-oxo species can result in the shift in the energy of the O→ Fe(III) CT transition to lower values. The absorption maximum at about 28 000 – 31 000 cm^{-1} could thus be connected with the dinuclear Fe(III)-O_n-Fe(III) complex or another defined polynuclear Fe(III)-oxo complex and the presence of absorption bands in lower energy at about 25 000 cm^{-1} reflects larger polynuclear Fe-oxo species.[34] High-energy absorptions of Fe ions above 33 000 cm^{-1} have been attributed to isolated Fe(III) ions with a frequency reflecting their coordination. Bordiga et al.[33] used isomorphous substitution of a small fraction of Si(IV) with Fe(III) in silicalite to obtain T_d-coordinated Fe(III) and subsequent high temperature treatment leading to the formation of extraframework O_h-coordinated Fe(III).

Table 3 Phase compositions and Fe_2O_3 crystallite size of prepared samples.

Catalyst	Fe	Phase content (%)				crystallite size(nm)				Amorphous
	(%)	δ	ϑ	α	Fe_2O_3	δ	ϑ	α	Fe_2O_3	phase
5Fe/Al_2O_3-A	5.27	20	70	8	2.0	9	9	5	7	w
5Fe/Al_2O_3-A/12	5.27	1	74	21	2.8	9	9	9	9	w
10Fe/Al_2O_3-A	10.22	2	51	43	4.2	9	8	5	7	v. w.
10Fe/Al_2O_3-A/12	10.22	1	22	72	5.3	9	10	9	17	v. w.
1Fe/Al_2O_3-B	0.85	2	42	55	0.3	8	8	17	10	w
4Fe/Al_2O_3-B	4.01	1	30	68	0.7	14	10	16	10	v. w.
9Fe/Al_2O_3-B	8.78	1	26	69	4	10	13	12	11	v. w.
9Fe/Al_2O_3-B/12	8.78	—	17	77	6	—	15	21	11	v. w.
4Fe/Al_2O_3-C	3.69	—	6	91	2.7	—	3	6	10	absent
Al_2O_3*	0.01	6	50	44	—	9	9	10	—	W

w – weak content 5 – 10%, v. w. – very weak content <5%

*Böhmite calcined at 1100 °C for 10 h in air.

On the bases of these experiments the absorption bands characteristic for T_d-coordinated Fe(III) have been found at about 47 000 and 42 000 cm^{-1}, O_h-coordinated Fe(III) species provided an intensive band at 36 000 – 38 000 cm^{-1}; however, accompanied also by an intensive absorption at higher energies.

Based on the literature data [3, 29, 32, 35-42], the presence of the absorption bands in the UV-Vis-NIR spectra in

50 000–31 000 cm^{-1} 31 000–18 000, and 18 000–4000 cm^{-1} regions can be assigned to the isolated Fe(III)-oxo species, oligomeric Fe species and iron oxide, respectively.

Fig. 4 shows that different types of alumina supports: A, B or C (with similar Fe content ~ 5 wt. %) yield significantly different band intensities in the spectral regions of the isolated Fe(III)-oxo species, Fe oligomers and iron oxides. This implies that the alumina support pretreatment influences the speciation of the Fe centres.

Fig. 5 shows UV-Vis-NIR spectra of catalyst B with different Fe content from 1 to 9 wt. %. The spectrum of $1Fe/Al_2O_3$-B shows broad absorptions bands in the high-energy region with the maxima at 38 000 and 46 000 cm^{-1}, which are characteristic of isolated Fe(III)-oxo species in octahedral coordination (O_h) and tetrahedral (T_d) coordination, respectively.[32-37, 43] The increase in Fe content (Fig. 5) to 4 wt.% results in a significant increase in the intensity of the absorption bands of isolated Fe(III)-oxo species (50 000–31 000 cm^{-1}), the appearance of a band at about 29 000 cm^{-1} reflects the formation of oligomeric Fe species, and an increase in the intensity of the weak absorption band with maximum at about 18 000 cm^{-1}

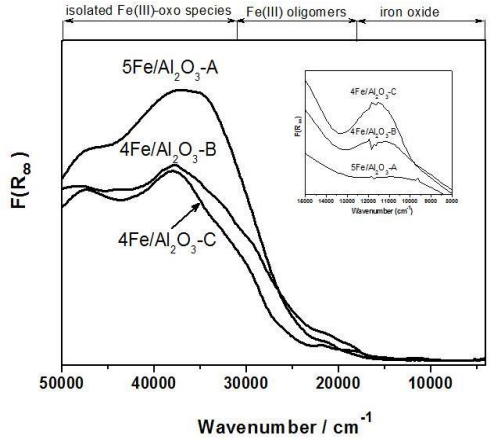

Fig. 4 UV-Vis-NIR diffuse reflectance spectra of hydrated Fe/Al_2O_3 catalysts prepared by A, B or C method with the similar (~ 5wt. %) Fe content.

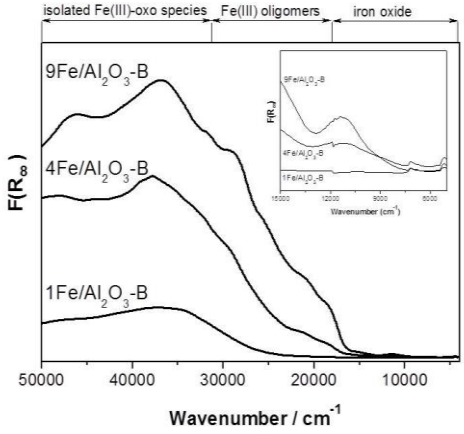

Fig. 5 UV-Vis-NIR diffuse reflectance spectra of hydrated Fe/Al_2O_3-B samples with different Fe content.

characteristic of Fe oxides.[32-34, 36, 37, 43, 44] The increase in the Fe content to 9 wt. % results in a significant increase and a shift of the absorption edge to 17 700 cm^{-1} being specific to the formation of more bulk Fe oxides (Fig. 5).[30, 33, 35, 36, 38, 39] The band at about 11 000 cm^{-1} observed at the samples with high Fe loading ($4Fe/Al_2O_3$-B and $9Fe/Al_2O_3$-B) is typical for Fe_2O_3 particles (Fig. 5).[33, 39, 42, 43]

The reflectance spectra of the aged samples of $4Fe/Al_2O_3$-B/12 and $10/Al_2O_3$-A/12 are shown in Fig. 6. Both samples show a significant increase in the intensity of the bands at 18 000 –

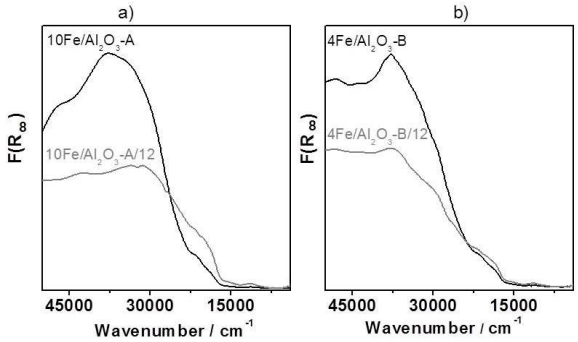

Fig. 6 Comparison of UV-Vis spectra of a) $4Fe/Al_2O_3$-B and b) $10Fe/Al_2O_3$-A showing the effect of 12 days aging in a stream of nitrous gases containing 15 vol.% of water vapor, 10 vol.% of NO and 1.5 vol.% of O_2 at 800 °C.

25 000 cm^{-1} characteristic of iron oligomers and iron oxide phase accompanied by a strong decrease in intensity of the broad absorption between 30 000 and 50 000 cm^{-1} corresponding to the isolated Fe(III)-oxo species. These clearly indicate that the aging leads to a partial redistribution of the iron species (the isolated Fe(III)-oxo or Fe(III) oligomers) from the highly dispersed forms to Fe oxides.[32, 38] Nevertheless, the absorption intensities in the spectrum of the treated $4Fe/Al_2O_3$-B at 30 000 – 50 000 cm^{-1} show that a part of Fe(III)-oxo species does not undergo such aggregation and Fe remains in its isolated form. The aged $10Fe/Al_2O_3$-A sample exhibited similar changes in the spectral features showing a decrease in the content of the dispersed Fe(III) ions. A higher intensity of the absorption edge at approximately 18 000 cm^{-1} compared to $4Fe/Al_2O_3$-B/12 reflects the presence of a high content of Fe-oxides.[32, 38]

The UV-Vis analysis showed heterogeneity in the structure and population of iron species in Fe/Al_2O_3 depending on the loading of Fe, contents of δ-, ϑ- and α-Al_2O_3 phases, and the ageing. Highly dispersed Fe(III)-oxo species in O_h and T_d coordination are predominantly present at a low Fe loading (1 wt. %) and on the δ-, ϑ-Al_2O_3 support (Fe/Al_2O_3-A). Well-dispersed Fe species show a clear tendency for the formation of oligomeric Fe species and Fe oxides at higher loadings and with the higher content of α-Al_2O_3. The aging results in a significant but not complete transformation of the isolated Fe(III)-oxo into Fe(III) oligomers and Fe oxides. A strong interaction between the Fe(III)-oxo species and the δ-, ϑ-Al_2O_3 support preserve part of these species from the aggregation.

3.4 Mössbauer spectroscopy

Mössbauer spectra of Fe/Al_2O_3 samples freshly prepared by the A, B and C methods and the sample after the aging process (4Fe-Al_2O_3-B/12) were recorded at room temperature and are shown in the Supplementary Information (Fig. S3). Their deconvolution was, however, rather complicated because of several overlapping doublets with very similar hyperfine parameters. These doublets originated from Fe species in the Al_2O_3 but also from the small particles of Fe oxides that are superparamagnetic at room temperatures. In order to distinguish them, we acquired the spectra at 4.2 K (Fig. 7, the solid lines show the best fit to the data), where the contributions from these Fe oxides (seen as doublets in the RT spectra) changed to sextets of magnetically ordered Fe-containing fraction. For their fitting a model with seven (eight) components: four sextets (S_n) and three (four) doublets (D_m) was applied. During the fitting procedure the linewidths of the doublets were left as free fitted parameters. The parameters from the deconvoluted low temperature Mössbauer spectra of Fe on Al_2O_3 support are collected in Table 4. Based on the literature data[45, 46], the sextet S1 with the isomer shift (IS) of 0.47–0.57 mm s^{-1}, quadrupole splitting (QS) less than 0 and the hyperfine field (B_{hf}) 51.1–53.5 T is attributed to the α-Fe_2O_3 (hematite) thin layers, nanoparticles or clusters with sizes <10 nm, where the Morin transition is suppressed.[47, 48] The sextet S2 with IS = 0.48–0.50 mm s^{-1}, QS > 0 and the B_{hf} = 53.4–54.1 T is ascribed to the α-Fe_2O_3 (hematite) thin layers or nanoparticles with the sizes > 10 nm below Morin transition.[47, 48] The sextet S3 with large linewidths and IS = 0.39–0.45 mm s^{-1}, QS = -0.11–0.00 mm s^{-1} and B_{hf} = 40.0–45.4 T and superparamagnetic relaxed sextet S4 with IS = 0.39–0.49 mm s^{-1}, QS = -0.14–0.19 mm s^{-1} and B_{hf} = 12.0–17.5 T are assigned to γ-Fe_2O_3 (maghemite).[49, 50] The typical values of doublet D1 for Fe(III) O_h coordination in α-Al_2O_3 (α-$Al_{2-x}Fe_xO_3$ (x = 0–0.1)) are IS = 0.39–0.42 mm s^{-1} and QS = 0.51–0.64 mm s^{-1}.[3, 7, 39-41, 51] The doublet D2 was attributed to Fe(III) in the T_d coordination in ϑ-Al_2O_3 (or possibly δ-Al_2O_3), where IS= 0.30–0.42 mm s^{-1} and QS= 1.11–1.30 mm s^{-1} [7, 34, 37] . The D3 components with the IS value between 0.68 and 0.72 mm s^{-1} and QS = 0.96-1.15 mm s^{-1} is characteristic for Fe(III) in O_h coordination in ϑ-Al_2O_3 (or δ-Al_2O_3). In Refs.[3, 7, 39-41, 51], a component with the Mössbauer parameters similar to D3 was assigned to the Fe oligomer species. The concentrations of the particular Fe sites depend on the preparation method. In all samples, Fe_2O_3 is the dominant (41–66%) fraction in the sextets S1-S4. The incorporation of Al(III) into hematite (sextets S1 and S2) slightly decreased the value of the hyperfine field. The sextets S1 and S2 were assigned to magnetically ordered α-Fe_2O_3 particles, layers or clusters present on the Al_2O_3 surface. The amount of Fe(III) in the T_d or O_h sites described by the D2 and D3 components varies between 6 and 26%. The contribution of the D2 and D3 components in aged 4Fe/Al_2O_3-B/12 compared to the non-aged 4Fe/Al_2O_3-B sample decreased from 16 to 13 %. To receive the good fitting parameters for Mössbauer spectrum of 4Fe/Al_2O_3-C prepared from amorphous aluminium oxide the component D4 (IS= 0.45 and QS= 1.56 mm/s) characterized Fe(III) was added. The presence of this component is connected with the different source of alumina than for series A and B.

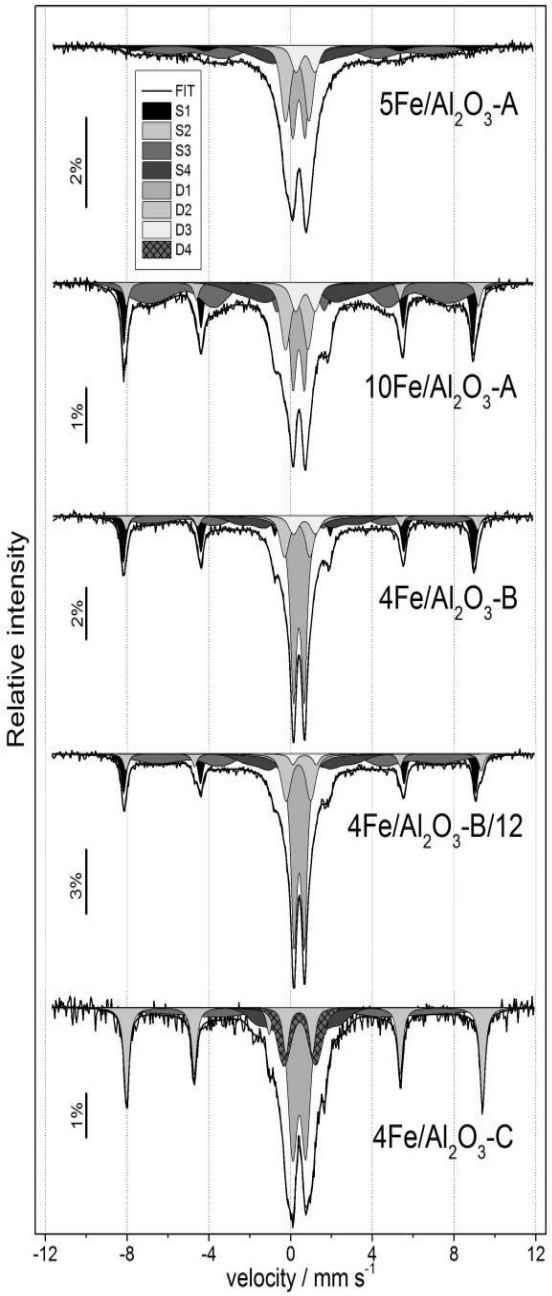

Fig. 7 Mössbauer spectra of Fe species in Fe/Al_2O_3 catalysts recorded at 4.2 K.

In contrast to Fe/Al_2O_3, the sample 10Fe/SiO_2 with negligible activity in the HT-deN_2O, displayed at 4.2 K Mössbauer spectrum with only sextets S1–S4 (Supplementary Information Fig. S4) indicating the presence of $Fe_{2-y}Si_yO_3$ particles in blocked state. The doublets in the spectrum at RT (see Supplementary Information, Fig. S5) thus correspond to these particles in the superparamagnetic state. Similarly the Fe(III) in nonmagnetic α-$Al_{2-x}Fe_xO_3$ (x = 0–0.1) giving rise to the doublet D1 was identified as not relevant for the catalytic activity (Supplementary Information, Table S2).

Journal Name

ARTICLE

Table 4 Mössbauer parameters and spectral contributions of Fe species in Fe/Al_2O_3 catalysts measured at 4.2 K.

Sample		IS (mm/s)	QS (mm/s)	B_{hf} (T)	Rel. (%)	Fe species
$5Fe/Al_2O_3$-A	S1	0.57	-0.06	51.1	8	m.o. α-Fe_2O_3 <10 nm
	S2	-	-	-	-	m.o. α-Fe_2O_3 >10 nm
	S3	0.44	0.00	40.6	28	m.o. γ-Fe_2O_3
	S4	0.44	0.19	13.0	18	m.o. γ-Fe_2O_3 (SP-relaxed)
	D1	0.39	0.60	-	20	Fe(III) O_h in α-$Al_{2-x}Fe_xO_3$
	D2	0.32	1.16	-	19	Fe(III) T_d
	D3	0.72	0.95	-	7	Fe(III) O_h
$10Fe/Al_2O_3$-A	S1	0.47	-0.18	53.1	15	m.o. α-Fe_2O_3 <10 nm
	S2	0.48	0.20	53.5	6	m.o. α-Fe_2O_3 >10 nm
	S3	0.43	-0.09	45.4	31	m.o. γ-Fe_2O_3
	S4	0.49	0.01	17.0	14	m.o. γ-Fe_2O_3 (SP-relaxed)
	D1	0.39	0.56	-	15	Fe(III) O_h in α-$Al_{2-x}Fe_xO_3$
	D2	0.30	1.11	-	13	Fe(III) T_d
	D3	0.72	0.96	-	6	Fe(III) O_h
$4Fe/Al_2O_3$-B	S1	0.48	-0.19	53.3	17	m.o. α-Fe_2O_3 <10 nm
	S2	0.49	0.13	53.4	5	m.o. α-Fe_2O_3 >10 nm
	S3	0.39	-0.11	45.1	17	m.o. γ-Fe_2O_3
	S4	0.39	0.05	17.5	12	m.o. γ-Fe_2O_3 (SP-relaxed)
	D1	0.39	0.53	-	33	Fe(III) O_h in α-$Al_{2-x}Fe_xO_3$
	D2	0.30	1.24	-	11	Fe(III) T_d
	D3	0.67	1.08	-	5	Fe(III) O_h
$4Fe/Al_2O_3$-B/12	S1	0.50	-0.14	53.5	13	m.o. α-Fe_2O_3 <10 nm
	S2	0.48	0.31	54.0	6	m.o. α-Fe_2O_3 >10 nm
	S3	0.45	-0.11	42.8	22	m.o. γ-Fe_2O_3
	S4	0.46	0.06	15.2	13	m.o. γ-Fe_2O_3 (SP-relaxed)
	D1	0.41	0.51	-	33	Fe(III) O_h in α-$Al_{2-x}Fe_xO_3$
	D2	0.38	1.22	-	11	Fe(III) T_d
	D3	0.68	1.15	-	2	Fe(III) O_h
$4Fe/Al_2O_3$-C	S1	-	-	-	-	m.o. α-Fe_2O_3 <10 nm
	S2	0.50	0.36	54.1	24	m.o. α-Fe_2O_3 >10 nm
	S3	0.40	-0.10	40.0	17	m.o. γ-Fe_2O_3
	S4	0.40	-0.14	12.0	12	m.o. γ-Fe_2O_3(SP-relaxed)
	D1	0.42	0.64	-	26	Fe(III) O_h in α-$Al_{2-x}Fe_xO_3$
	D2	0.42	1.30	-	6	Fe(III) T_d
	D3	-	-	-	-	Fe(III) O_h
	D4	0.45	1.56		15	Fe(III)

m.o. = magnetically ordered, SP-relaxed = superparamagnetically relaxed

Journal Name

ARTICLE

3.5 Summary of the structural features

The series of prepared Fe/Al_2O_3 catalysts represent a sequence of samples with a complex mixture of the metastable alumina phases relevant for the temperature region of the HT-N_2O elimination, and with the varying amount of the iron species stabilized on the alumina support under the HT-deN_2O conditions. The processes involved in the preparation, the iron content and the sample history and the exposure to various conditions with the dominant role of temperature and gas phase composition influence the final structural features of the individual samples. As evidenced by the XRD results, the size of the alumina crystallites is well within the nanometre-length scale, in particular between 6 and 17 nm, and two dominant metastable alumina polymorphs, which are relevant for the samples exposed to the process temperature, are δ and mostly ϑ phase, and the thermodynamically most stable high-temperature α-Al_2O_3 phase that can be detected in various proportions.

Under the specific conditions of the HT-deN_2O process there exists a complex interaction between the two catalysts components, i.e., the iron species and the alumina support, and the transformation of alumina to more stable forms is accelerated by the iron ions being embedded in the alumina structure and so that the temperature of the transformation to the α-phase is reduced.

The direct interaction between the iron and aluminium sources in the Fe/Al_2O_3-C catalyst has the accelerating effect noted in the above paragraph and results in an easier formation of the Fe_2O_3 phase. Therefore, both ϑ and δ alumina phase, which dominates in Fe/Al_2O_3-A and -B samples, appear to be the alumina modifications relevant to HT-deN_2O. It is probably significant that Fe(III) occupy both O_h and T_d coordination in ϑ and δ alumina.

Speciation of Fe in Al_2O_3 was confirmed by two complementary methods UV-Vis and Mössbauer spectroscopy. UV-Vis results confirmed that iron in Al_2O_3 is present as isolated Fe-oxo species (T_d or O_h coordination), Fe(III)-oxo oligomers and iron oxide particles. All three forms are present in all prepared samples. Aging led to transformation of Fe(III)-oxo and Fe(III)-oxo oligomers to iron oxides. Mössbauer analysis confirmed the presence of isolated Fe(III) of either $T_d$or O_h coordination (probably stabilized at the alumina surface defects), small iron oxide crystallites and finally bulk particles of iron oxide of the developed Fe_2O_3 structure. Assuming, that iron structures present in Fe/SiO_2 are different types of iron oxides (Table S2), thus these structures are not active in HT-N_2O decomposition (Supplementary Information Fig. S6).

The distribution of the individual iron species is influenced by several parameters, such as the process of catalysts preparation, the resulting alumina support modifications and the iron content.

3.6 Catalytic results

The comparison of three types of catalysts with the same concentration level of Fe (Fe content of 4–5 wt.%), reveals the high performance of the Fe/Al_2O_3-A and Fe/Al_2O_3-B catalysts and lower activity of the Fe/Al_2O_3-C catalyst (Fig. 8a). Nevertheless, all Fe/Al_2O_3 measured in this work are superior to the iron catalyst based on the SiO_2 (Supplementary Information Fig. S6). On the other hand, the pure alumina used as catalyst exhibited very low catalytic activity in HT-N_2O decomposition caused by the presence of iron traces (Table 5). The activity increases with the total iron content rising from 1 to 4 wt. %. Catalytic activity results showed that the concentration of Fe over Al_2O_3 above 5 wt. % does not improve the catalytic performance (Table 5 and Fig. 8b).

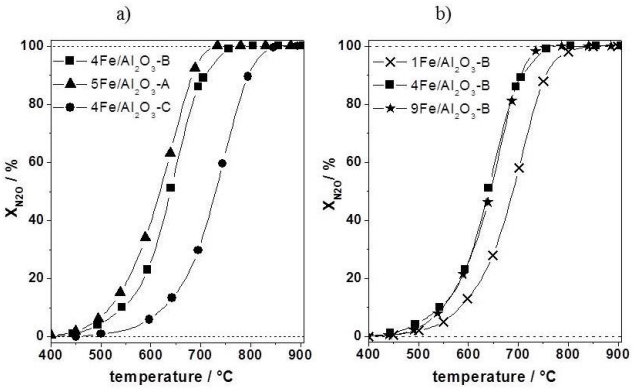

Fig. 8 Effect of alumina supports on the conversion of N_2O as a function of temperature over Fe/Al_2O_3 catalysts a) prepared by method A, B and C with a similar Fe content ~ 4 wt. % and, b) different Fe loadings in the samples prepared by method B.

Accordingly, based on the low performance of the Fe/Al_2O_3-C sample, the preparation method based on the interaction of Fe/Al_2O_3 using amorphous AlO(OH) suspension does not provide a suitable catalyst for the HT-deN_2O process. Catalytic experiments are performed at the constant GHSV and the measurements have the identical hydrodynamic (regime) conditions. For the purpose of analyzing the relationship between the structural properties and catalytic activity, the primary data are reprocessed at constant WHSV (see Table 5) (in details Supplementary Information, chapters 4 and 5).

The catalytic tests were systematically performed in a complex gas mixture simulating the industrial stream also including the NO gas. As shown by additional experiments, the catalytic activity (here shown for the $4Fe/Al_2O_3$-B catalyst) is not

strongly influenced by the presence of NO (see Supplementary Information, Fig. S7) in the high-temperature range (750–930 °C) relevant for the industrial application. Some positive effects of NO presence are only identified at lower temperatures. This would be in strong contradiction to the results obtained with the zeolite-based iron catalysts, where the positive NO role is well-documented.[52-54]

Comparison of the performances of the A and B types of catalysts before and after aging (Fig. 9) shows that they exhibit relatively good resistance to long-term exposure to the HT-deN_2O process reaction conditions.

Table 5 Calculated parameters of kinetic experiments: the normalized temperature of 50% conversion (T_{X50}), the conversion at 650 °C (X_{650}), the apparent kinetic parameters (E_A – the activation energy, k_A – the rate constant), the initial reaction rate ($R_{N2O} = k_A\, p^0_{N2O}$) at T = 650 °C.

Catalyst	T_{X50} (°C)	X_{650} (%)	k_{ref} (nmol $Pa^{-1}s^{-1}g^{-1}$)	E_A (kJ mol^{-1})	R_{N2O} (μmol $s^{-1}g^{-1}$)
5Fe/Al_2O_3-A	650	50.6	16.9	119.3	1.71
10Fe/Al_2O_3-A	656	45.8	14.6	152.3	1.48
10Fe/Al_2O_3-A/12d	673	35.4	10.5	144.1	1.06
1Fe/Al_2O_3-B	728	16.1	4.2	135.8	0.42
4Fe/Al_2O_3-B	678	33.9	9.9	133.2	1.00
4Fe/Al_2O_3-B/12d	708	24.7	6.8	116.8	0.69
9Fe/Al_2O_3-B	687	29.2	8.3	137.5	0.84
9Fe/Al_2O_3-B/12d	730	14.1	3.6	148.5	0.37
4Fe/Al_2O_3-C	759	8.8	2.2	146.4	0.22
Al_2O_3*	843	1	0.1	188.6	0.01

*Böhmite calcined at 1100 °C for 10 h in air.

In order to analyse the catalytic performance of Fe-alumina catalysts the kinetic studies based on either the temperature of 50% N_2O conversion (T_{X50}) at WHSV regime (Supplementary Information, chapters 4 and 5) or the value of the rate constant k_{ref} at reference temperature 650°C (Table 5) was applied. As confirmed by Pérez-Ramírez *et al.*[53-57], the rate of N_2O decomposition on Fe-catalysts can be considered as the first-order with respect to the N_2O partial pressure. The same kinetic regime is assumed for all experiments, which is supported by the following evidences: (i) external mass and heat transport effects were examined by experiments with varying catalyst mass at constant GHSV and (ii) internal mass transfer has insignificant effect on the estimated parameters (< 5 kJ mol^{-1} in E_A). Using the obtained catalytic data, the apparent kinetic parameters, the activation energy E_A and the rate constant at reference temperature k_{ref} were estimated by a weighted non-linear regression of the experimental data using plug-flow reactor (PFR) model of the reactor in the following differential form:

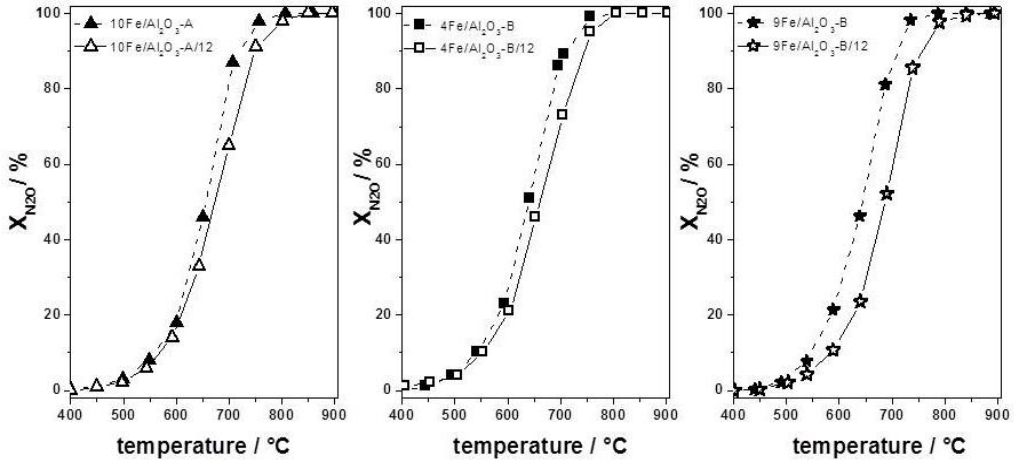

Fig. 9 Effect of aging of a) 10Fe/Al_2O_3-A, b) 4Fe/Al_2O_3-B, and c) 9Fe/Al_2O_3-B on the conversion of N_2O as a function of temperature. Hydrothermal aging was performed in a stream of nitrous gases containing 15 vol.% of water vapor, 10 vol.% of NO and 1.5 vol.% of O_2 at 800 °C for 12 days.

$$\frac{\mathrm{d}F_{\mathrm{N_2O}}}{\mathrm{d}w} = -m_{\mathrm{cat}} k_{\mathrm{ref}} \exp\left\{-\frac{E_{\mathrm{A}}}{\mathbf{R}T_{\mathrm{ref}}}\left(\frac{T_{\mathrm{ref}}}{T}-1\right)\right\} p_{\mathrm{N_2O}} \qquad (1)$$

where $F_{\mathrm{N_2O}}$ – is the N_2O molar flow, w – is the dimensionless catalyst mass, m_{cat} – the catalyst mass, T_{ref} – is the reference temperature (923 K or 650 °C), and $p_{\mathrm{N_2O}}$ – is the N_2O partial pressure.

Among the studied catalysts, Fe/Al_2O_3-A exhibited the lowest T_{X50} with the highest k_{ref} values. For all Fe-Al_2O_3 the aging led to increasing of T_{X50} from 20 to 40 °C (Table 5). The calculated activation energy varies in the range of 120–150 kJ mol^{-1}, which are typical for Fe/Al_2O_3-based catalysts.[11, 12, 16] Only for Fe/Al_2O_3-A, the E_A value varies by about 30 kJ mol^{-1} (with different iron contents), while for Fe/Al_2O_3-B there is no evident dependence of E_A on Fe content. It indicates that the aging does not substantially influence E_A values.

3.7. Structure-catalytic activity relationship

Combining the present results for the structuralcharacterization and catalytic properties of Fe/Al_2O_3 allows a detailed discussion of the relationship between the existing Fe centres and their relevance for the activity in the HT-deN_2O process.

The Fe/SiO_2 catalyst showed very low activity for HT-deN_2O reaction and it indicated that the presence of iron species in Fe/SiO_2 (Supplementary Information Table S2 and Fig. S6) has negligible relevance for the HT-deN_2O. Bulk Fe_2O_3 and superparamagnetic (at RT) small clusters of iron oxides, both present in Fe/SiO_2 and Fe/Al_2O_3 materials are thus excluded as the principal active sites in HT-deN_2O. However, Fe species in the T_d or O_h coordination or in the form of oligomers in Fe/Al_2O_3 were suggested to be the potential active iron centres in HT-deN_2O. The analogical iron structures, both adjacent to Al atoms, were proposed as active sites for effective decomposition of N_2O over Fe-zeolites.[3, 7, 51, 58, 59] These two iron structures are more abundant in Fe/Al_2O_3 samples with higher content of the metastable alumina phases: δ or ϑ. The concentration of Fe(III) in T_d or O_h coordination or the content of Fe(III) oligomers decrease with the transformation of the alumina support into α phase. This transformation is accelerated by the presence of iron ions that actually decrease the temperature of ϑ to α transformation in catalysts with higher intermixing between Fe and Al_2O_3.

Fig. 10 showed the correlation between the concentration of Fe(III) in T_d and O_h coordination (Supplementary Information, Table S4) suggested as active sites and the rate of HT-deN_2O decomposition at 650 °C (Table 5). These results indicated a correspondence between the amount of the Fe(III) species and their participation in the HT-deN_2O process.

The highest rate of N_2O decomposition was exhibited by Fe/Al_2O_3-A which contained the highest Fe(III) concentration. After the aging of $4Fe/Al_2O_3$-B, the amount of Fe(III) decreased from 0.114 ($4Fe/Al_2O_3$-B) to 0.093 mmol g^{-1} ($4Fe/Al_2O_3$-B/12) which is reflected in the decrease of the catalytic activity of the aged sample $4Fe/Al_2O_3$-B/12 in comparison with $4Fe/Al_2O_3$-B. Sample $4Fe/Al_2O_3$-C containing the highest amount of α phase of Al_2O_3 and the lowest concentration of Fe(III) displayed the lowest activity in HT-deN_2O among all studied catalysts. By combination of catalytic results with the physicochemical characterization it was shown that the catalytic performance of Fe/Al_2O_3 can be tuned by increasing the concentration of the δ-, ϑ-Al_2O_3 responsible for stabilization of Fe(III) in Td or Oh coordination active in transformation N_2O to O_2 and N_2.

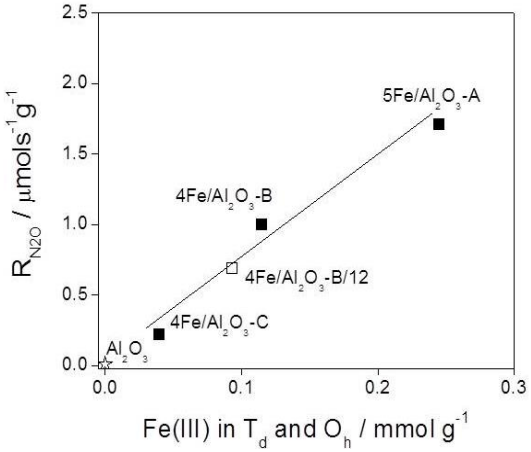

Fig. 10 Rate at 650 °C of N_2O decomposition as function of concentration of Fe(III) in T_d an O_h coordination over Fe/Al_2O_3 with similar content of Fe (~ 4% wt.).

4. Conclusions

Three types of Fe/Al_2O_3 catalysts were prepared by different preparation routes (A, B, and C) which are potentially relevant for the preparation of suitable catalytic materials for HT-deN_2O process in the technology of nitric acid production. Two types started from commercial böhmite impregnating alumina supports by ammonium iron (III) citrate (A and B) and one from amorphous AlO(OH) where Fe was introduced by acidic $FeCl_2$ solution (C).

Different preparation routes resulted in the presence of different phases of the alumina support as well as the iron species. The presence of iron ions influenced the transformation of alumina phases and the role of the actual alumina modifications in the stabilization of the specific iron species was crucial for the activity of Fe/Al_2O_3 catalysts in HT-deN_2O.

Based on our study of Fe/SiO_2 material containing non-active Fe forms, all the prepared Fe/Al_2O_3 contained two iron species active in the HT-deN_2O reaction, in particular Fe(III) in T_d or O_h coordination. The presence of various alumina phases with relatively high surface area even in the temperature region of the decomposition process was necessary for the stabilization of the active iron species. Transformation of the alumina support into α modification has principally negative effect during aging.

The rate of this transformation increases with the increasing total content of iron in catalysts with higher intermixing between Fe and Al_2O_3. Thus, the catalytic stability is connected to long-term preservation of ϑ (δ) Al_2O_3 modifications in the temperature region of the reaction.

Impregnation of the pre-calcined böhmite at 1100 °C (Fe/Al_2O_3-B), already preformed δ/ϑ alumina support, provided samples which had highly stable distribution of the relevant iron species also during the long-term exposition to the reaction conditions.

Conflicts of interest

There are no conflicts to declare.

Acknowledgements

The authors acknowledge the assistance provided by the Research Infrastructure NanoEnviCz, supported by the Ministry of Education, Youth and Sports of the Czech Republic under Project No. LM2015073 and Czech Science Foundation for the financial support under project GA14-10251S and by RVO# 61388955.

Notes and references

1. J. Perez-Ramirez and E. V. Kondratenko, *Catal. Today*, 2007, **121**, 160-169.
2. J. Perez-Ramirez, *Appl. Catal. B.*, 2007, **70**, 31-35.
3. E. Tabor, G. Sádovská, M. Bernauer, P. Sazama, J. Nováková, V. Fíla, T. Kmječ, J. Kohout, K. Závěta and Z. Sobalík, *Appl. Catal. B.*, 2017.
4. L. Chmielarz, M. Rutkowska, M. Jablonska, A. Wegrzyn, A. Kowalczyk, P. Boron, Z. Piwowarska and A. Matusiewicz, *Appl. Clay. Sci.*, 2014, **101**, 237-245.
5. M. Ruszak, M. Inger, S. Witkowski, M. Wilk, A. Kotarba and Z. Sojka, *Catal. Lett.*, 2008, **126**, 72-77.
6. G. Giecko, T. Borowiecki, W. Gac and J. Kruk, *Catal. Today*, 2008, **137**, 403-409.
7. G. Sadovska, E. Tabor, P. Sazama, M. Lhotka, M. Bernauer and Z. Sobalik, *Catal. Commun.*, 2017, **89**, 133-137.
8. M. Konsolakis, *ACS Catal.*, 2015, **5**, 6397-6421.
9. L. G. Pinaeva, I. P. Prosvirin, L. S. Dovlitova, I. G. Danilova, E. M. Sadovskaya and L. A. Isupova, *Catal. Sci. Technol.*, 2016, **6**, 2150-2161.
10. P. Pomonis, D. Vattis, A. Lycourghiotis and C. Kordulis, *J. Chem. Soc., Faraday Trans.*, 1985, **81**, 2043-2051.
11. A. K. Ladavos and T. V. Bakas, *React. Kinet. Catal. Lett.*, 2001, **73**, 223-228.
12. A. K. Ladavos and T. V. Bakas, *React. Kinet. Catal. Lett.*, 2001, **73**, 229-235.
13. M. Haneda, M. Shinriki, Y. Nagao, Y. Kintaichi and H. Hamada, *Bull. Chem. Soc. Jpn.*, 2003, **76**, 2329-2333.
14. G. Pekridis, C. Athanasiou, M. Konsolakis, I. V. Yentekakis and G. E. Marnellos, *Top. Catal.*, 2009, **52**, 1880-1887.
15. A. Gervasini and M. Marzo, *Adsorpt. Sci. Technol.*, 2011, **29**, 365-379.
16. J. Kruk, K. Stolecki, K. Michalska, M. Konkol and P. Kowalik, *Catal. Today*, 2012, **191**, 125-128.
17. A. Boubnov, A. Roppertz, M. D. Kundrat, S. Mangold, B. Reznik, C. R. Jacob, S. Kureti and J. D. Grunwaldt, *Appl. Surf. Sci.*, 2016, **386**, 234-246.
18. A. Tomita, T. Miki, T. Tango, T. Murakami, H. Nakagawa and Y. Tai, *ChemPhysChem*, 2015, **16**, 2015-2020.
19. J. Gangwar, B. K. Gupta, S. K. Tripathi and A. K. Srivastava, *Nanoscale*, 2015, **7**, 13313-13344.
20. I. Levin and D. Brandon, *J. Am. Ceram. Soc.*, 1998, **81**, 1995-2012.
21. J. A. Jimenez, I. Padilla, A. Lopez-Delgado, L. Fillali and S. Lopez-Andres, *Int. J. Appl. Ceram. Technol.*, 2015, **12**, E178-E186.
22. Y. C. Xie, X. P. Xu, B. Y. Zhao, Y. C. Tang and G. B. Wu, *Catal. Lett.*, 1992, **13**, 239-245.
23. N. C. Halder and C. N. J. Wagner, *Acta Crystallogr.*, 1966, **20**, 312-313.
24. L. Kovarik, M. Bowden, D. C. Shi, N. M. Washton, A. Andersen, J. Z. Hu, J. Lee, J. Szanyi, J. H. Kwak and C. H. F. Peden, *Chem. Mater.*, 2015, **27**, 7042-7049.
25. G. C. Bye and G. T. Simpkin, *J. Am. Ceram. Soc.*, 1974, **57**, 367-371.
26. J. M. Andersson, E. Wallin, V. Chirita, E. P. Munger and U. Helmersson, *Phys. Rev. B: Condens. Matter*, 2005, **71**.
27. E. Wallin, J. M. Andersson, V. Chirita and U. Helmersson, *J. Phys.: Condens. Matter*, 2004, **16**, 8971-8980.
28. A. Alberti and A. Martucci, *Microporous Mesoporous Mater.*, 2011, **141**, 192-198.
29. L. Capek, V. Kreibich, J. Dedecek, T. Grygar, B. Wichterlova, Z. Sobalik, J. A. Martens, R. Brosius and V. Tokarova, *Microporous Mesoporous Mater.*, 2005, **80**, 279-289.
30. P. Sazama, O. Bortnovsky, J. Dedecek, Z. Tvaruzkova and Z. Sobalik, *Catal. Today*, 2011, **164**, 92-99.
31. I. V. Chernyshova, S. Ponnurangam and P. Somasundaran, *Phys.Chem.Chem.Phys.*, 2010, **12**, 14045-14056.
32. G. D. Pirngruber, P. K. Roy and R. Prins, *Phys.Chem.Chem.Phys.*, 2006, **8**, 3939-3950.
33. S. Bordiga, R. Buzzoni, F. Geobaldo, C. Lamberti, E. Giamello, A. Zecchina, G. Leofanti, G. Petrini, G. Tozzola and G. Vlaic, *J. Catal.*, 1996, **158**, 486-501.
34. N. Amin and S. Arajs, *Phys. Rev. B: Condens. Matter*, 1987, **35**, 4810-4811.
35. J. Dedecek, L. Capek, P. Sazama, Z. Sobalik and B. Wichterlova, *Appl .Catal. A*, 2011, **391**, 244-253.
36. L. Capek, J. Dedecek, P. Sazama and B. Wichterlova, *J. Catal.*, 2010, **272**, 44-54.
37. Z. Sobalik, P. Sazama, J. Dedecek and B. Wichterlova, *Appl .Catal. A*, 2014, **474**, 178-185.
38. P. Sazama, Z. Sobalik, J. Dedecek, I. Jakubec, V. Parvulescu, Z. Bastl, J. Rathousky and H. Jirglova, *Angew. Chem. Int. Ed.*, 2013, **52**, 2038-2041.
39. P. Sazama, N. K. Sathu, E. Tabor, B. Wichterlova, S. Sklenak and Z. Sobalik, *J. Catal.*, 2013, **299**, 188-203.

40. E. Tabor, K. Zaveta, N. K. Sathu, A. Vondrova, P. Sazama and Z. Sobalik, *Catal. Today*, 2011, **175**, 238-244.
41. E. Tabor, K. Zaveta, N. K. Sathu, Z. Tvaruzkova and Z. Sobalik, *Catal. Today*, 2011, **169**, 16-23.
42. J. Kiwi, N. Denisov, Y. Gak, N. Ovanesyan, P. A. Buffat, E. Suvorova, F. Gostev, A. Titov, O. Sarkisov, P. Albers and V. Nadtochenko, *Langmuir*, 2002, **18**, 9054-9066.
43. K. Jíša, J. Nováková, M. Schwarze, A. Vondrová, S. Sklenák and Z. Sobalik, *J. Catal.*, 2009, **262**, 27-34.
44. P. Sazama, R. Pilar, L. Mokrzycki, A. Vondrova, D. Kaucky, J. Plsek, S. Sklenak, P. Stastny and P. Klein, *Appl. Catal. B.*, 2016, **189**, 65-74.
45. P. Liu, S. He, H. Wei, J. Wang and C. Sun, *Ind. Eng. Chem. Res.*, 2015, **54**, 130-136.
46. S. P. M. Ristić, S. Musić, *Croat. Chem. Acta*, 2009, **397–404**.
47. H. M. Lu and X. K. Meng, *J. Phys. Chem. C*, 2010, **114**, 21291-21295.
48. R. E. Vandenberghe, E. De Grave, C. Landuydt and L. H. Bowen, *Hyperfine Interact.*, 1990, **53**, 175-195.
49. J. Tucek, R. Zboril and D. Petridis, *Journal of Nanoscience and Nanotechnology*, 2006, **6**, 926-947.
50. A. G. Roca, J. F. Marco, M. d. P. Morales and C. J. Serna, *J. Phys. Chem. C*, 2007, **111**, 18577-18584.
51. Z. Sobalik, J. Novakova, J. Dedecek, N. K. Sathu, E. Tabor, P. Sazama, P. Stastny and B. Wichterlova, *Microporous Mesoporous Mater.*, 2011, **146**, 172-183.
52. J. Nováková and Z. Sobalík, *Catal. Lett.*, 2006, **111**, 195-202.
53. J. Pérez-Ramírez and F. Kapteijn, *Appl. Catal. B.*, 2004, **47**, 177-187.
54. J. Perez-Ramirez and F. Kapteijn, *Catal. Commun.*, 2003, **4**, 333-338.
55. G. Mul, M. W. Zandbergen, F. Kapteijn, J. A. Moulijn and J. Perez-Ramirez, *Catal. Lett.*, 2004, **93**, 113-120.
56. J. Perez-Ramirez, F. Kapteijn, K. Schoffel and J. A. Moulijn, *Appl. Catal. B.*, 2003, **44**, 117-151.
57. J. Perez-Ramirez, F. Kapteijn and A. Bruckner, *J. Catal.*, 2003, **218**, 234-238.
58. P. Sazama, B. Wichterlová, E. Tábor, P. Šťastný, N. K. Sathu, Z. Sobalík, J. Dědeček, Š. Sklenák, P. Klein and A. Vondrová, *J. Catal.*, 2014, **312**, 123-138.
59. P. Sazama, N. K. Sathu, E. Tabor, B. Wichterlová, Š. Sklenák and Z. Sobalík, *J. Catal.*, 2013, **299**, 188-203.